Science of the Total Environment 636 (2018) 1520–1533

Contents lists available at ScienceDirect

Science of the Total Environment

journal homepage: www.elsevier.com/locate/scitotenv

Influence of recent climatic events on the surface water storage of the Tonle Sap Lake

F. Frappart [a,b,*], S. Biancamaria [b], C. Normandin [c], F. Blarel [b], L. Bourrel [a], M. Aumont [b], P. Azemar [b], P.-L. Vu [a], T. Le Toan [d], B. Lubac [c], J. Darrozes [a]

[a] Géosciences Environnement Toulouse (GET), UMR 5563, CNRS/IRD/Université de Toulouse, OMP-GRGS, 14 Avenue Edouard Belin, 31400 Toulouse, France
[b] LEGOS, Université de Toulouse, CNES, CNRS, IRD, UPS - 14 avenue Edouard Belin, 31400 Toulouse, France
[c] Environnement et Paléo-Environnement Océaniques et Continentaux (EPOC), UMR 5805, CNRS/Université de Bordeaux, Allée Geoffroy Saint-Hilaire, 33615 Pessac, France
[d] Centre d'Etudes Spatiales de la Biosphère (CESBIO), UMR 5126,CNRS/CNES/IRD/Université de Toulouse, 13 Avenue du Colonel Roche, 31400 Toulouse, France

HIGHLIGHTS

- Temporal evolution of the surface water storage of the Tonle Sap lake over 1993–2017 in response to climate variability
- Extreme droughts and floods are observed during large ENSO events enhanced by PDO
- Flood of 2002 and drought of 2016 were also respectively due to the persistence of wet and dry periods from previous years
- A first assessment of the impact of the extreme drought of 2015 on the Tonle Sap ecosystem is also presented

GRAPHICAL ABSTRACT

Interannual variations of monthly surface water volume of the Tonle Sap watershed (a), anomalies of ENSO 3.4 (b) and PDO (c) indices over 1997–2017.

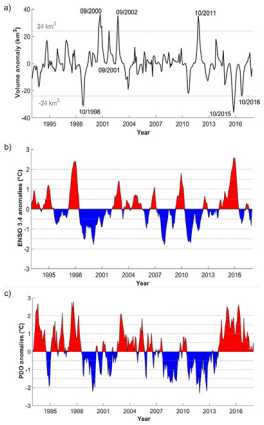

ARTICLE INFO

Article history:
Received 25 October 2017
Received in revised form 23 April 2018
Accepted 24 April 2018
Available online 7 May 2018

Keywords:
Surface water storage
Rainfall
ENSO
PDO
Monsoon
EVI
Mekong Basin
Multi-satellite

ABSTRACT

Lakes and reservoirs have been identified as sentinels of climate change. Tonle Sap is the largest lake in both the Mekong Basin and Southeast Asia and because of the importance of its ecosystem, it is has been described as the "heart of the lower Mekong". Its seasonal cycle depends on the annual flood pulse governed by the flow of the Mekong River. This study provides an impact analysis of recent climatic events from El Niño 1997/1998 to El Niño 2015/2016 on surface storage variations in the Tonle Sap watershed determined by combining remotely sensed observations, multispectral images and radar altimetry from 1993 to 2017. The Lake's surface water volume variations are highly correlated with rainy season rainfall in the whole Mekong River Basin ($R = 0.84$) at interannual time-scale. Extreme droughts and floods can be observed when precipitation deficit and excess is recorded in both the Tonle Sap watershed and the Mekong River Basin during moderate to very strong El Niño/La Niña events ($R = -0.70$) enhanced by the Pacific Decadal Oscillation ($R = -0.68$). Indian and Western North Pacific Monsoons were identified as having almost equal influence. Below normal vegetation activity was observed during the first semester of 2016 due to the extreme drought in 2015.

* Corresponding author at: Géosciences Environnement Toulouse (GET), UMR 5563, CNRS/IRD/Université de Toulouse, OMP-GRGS, 14 Avenue Edouard Belin, 31400 Toulouse, France
E-mail address: frederic.frappart@legos.obs-mip.fr (F. Frappart).

https://doi.org/10.1016/j.scitotenv.2018.04.326
0048-9697/

1. Introduction

Climate variability and human population growth have led to inland waters being identified as some of the most severely endangered ecosystems (Rosenzweig et al., 2007). Lakes and reservoirs are widely distributed around the world and act as integrators of changes occurring in their watershed, the surrounding landscape and the atmosphere (Schindler, 2009; Williamson et al., 2009a). As their physical, chemical, and biological properties respond rapidly to climate-induced changes, they offer a valuable source of information for assessing and monitoring the effects of climate change (e.g., Magnuson, 2000; Lemoalle et al., 2012). Lakes and reservoirs are commonly seen as sentinels of climate change as their physical, chemical, and biological responses to climate variations integrate the changes occurring in their catchment (Adrian et al., 2009; Schindler, 2009; Williamson et al., 2009a,b).

Tonle Sap Lake in Cambodia is the largest lake and wetland ecosystem in the Mekong River Basin (MRC, 2005). It is considered as the "heart of the Lower Mekong" due to the exceptional biodiversity of its ecosystem (Campbell et al., 2006) and is also one of the most productive ecosystems in the world (Lamberts, 2006) with its high productivity being linked to the flood pulse of the Mekong River (Kummu et al., 2006). The hydrological cycle in the Mekong River Basin is governed by the monsoon regime, itself being strongly influenced by El Niño Southern Oscillation (ENSO). El Niño events are responsible for a decrease in the rainfall, discharge and annual flood period (Räsänen and Kummu, 2013). Conversely, La Niña increases the rainfall, discharge and annual flood period. The combination of climate-related and anthropogenic (hydropower, irrigation) changes in the Mekong River Basin are expected to cause large modifications to the flood pulse of the Tonle Sap (Kummu and Sarkkula, 2008; Västilä et al., 2010). The frequency and intensity of drought and flood events in the region have increased over the past few decades, impacting irrigated fields (Cruz et al., 2007; Kamoshita and Ouk, 2015). Dam construction and operations in the Chinese Upper Mekong Basin are also altering the hydrological regime in the Lower Mekong Basin (Stone, 2010; Lu et al., 2014). Development of new hydropower dams in the Chinese Upper Mekong Basin combined with possible development of thirty-eight new dams in the Vietnamese Lower Mekong Basin will have a major impact on the hydrological regime of this region (see Lu et al., 2014 for the impacts on the Chinese Upper Mekong Basin; Arias et al., 2014 for the impacts on the Vietnamese Lower Mekong Basin).

Remotely sensed observations offer a unique opportunity to continuously monitor floods in large watersheds. Previous studies have determined spatio-temporal flooding extent by applying a threshold approach to land surface reflectances, or spectral indexes from the MODerate resolution Imaging Sensor (MODIS) radiometer (Sakamoto et al., 2007; Arias et al., 2012; Siev et al., 2016; Fayne et al., 2017) in the Tonle Sap watershed. Gravity Recovery and Climate Experiment (GRACE) products have recently been used along with MODIS images to estimate total water storage and identify flood events in the Tonle Sap watershed (Tangdamrongsub et al., 2016). Estimates of surface water volume changes in the Tonle Sap watershed are sparse and have only been for short time-periods (e.g., 1997–2005 in Kummu and Sarkkula, 2008; and 2003–2005 in Siev et al., 2016).

The purpose of this study is to estimate Tonle Sap lake storage variations over the two last decades and analyze the link between its annual variations with atmospheric forcing, especially climatic oscillations. Surface water storage variations of the lake are computed over the 1993–2017 time span, through a synergistic use of flood extent derived from MODIS land surface reflectances (see Sections 3.1 and 4.1) and altimetry-based water levels (see Sections 3.2 and 4.2). During these two decades, three extreme droughts (1998, 2015, and 2016) and three exceptional floods (2000, 2002, and 2011) occurred in the Tonle Sap watershed. In the following, relationships with climate variability are discussed through comparisons with climate indices (Sections 3.3 and 5.2). A first impact assessment of the extreme drought of 2015 on the Tonle Sap ecosystem is also presented.

2. Study area

Ninety-five percent of the Tonle Sap Lake drainage area is located in Cambodia, with the remaining 5% in Thailand. It is the largest lake and wetland in the Mekong River Basin and the largest lake in Southeast Asia (MRC, 2005; Campbell et al., 2009). Its whole drainage basin occupies an area of 85,800 km^2 (i.e., 11% of the whole surface of the Mekong basin, MRC, 2003) (Fig. 1). The lake-floodplain system extends from 2400 km^2 during the low water period to 16,000 km^2 at peak flood during wet years (Lim et al., 1999; Kummu and Sarkkula, 2008).

The catchment incorporates five different land cover classes, as described by Arias et al. (2012):

- Open water (under water from 9 to 12 months a year and covering an area of 3027 km^2),
- Gallery forest (annually flooded for 9 months and covering an area of 197 km^2)
- Seasonally flooded habitats, composed of shrublands and grasslands (annually flooded from 5 to 8 months on average and covering an area of 5409 km^2)
- Transitional habitats dominated by abandoned agricultural fields, receding rice/floating rice, and lowland grasslands (annually flooded from 1 to 5 months on average and covering an area of 3658 km^2)
- Rainfed habitats mostly composed of wet season rice fields and village crops (flooded <1 month per year and covering an area of 8641 km^2)

Tonle Sap Lake is an important ecosystem of Southeast Asia due to its exceptional biodiversity (Campbell et al., 2006). It has been internationally recognized through three Biosphere Reserve core areas under the United Nations Educational, Scientific and Cultural Organization (UNESCO) Programme on Man and the Biosphere (UNESCO, 2006), as well as one Ramsar site under the Ramsar Convention on wetlands (see www.ramsar.org). The Tonle Sap lake ecosystem also supports important fisheries and aquaculture activities. These industries sustain over one million people (Rainboth, 1996; Sverdrup-Jensen, 2002; Hortle, 2007).

The annual monomodal flood pulse in Tonle Sap Lake is governed by the flow in the Mekong River (Junk et al., 2006; Lamberts, 2006). The Tonle Sap River connects the lake to the Mekong River. In the May to September wet season its flow direction is inversed due to water level increase in the Mekong River (Kummu and Sarkkula, 2008). Annual average inflow and outflow are 79.0 and 78.6 km^3, respectively. 57% of the inflow comes from the Mekong mainstem, either through Tonle Sap River discharge (52%) or by overland flooding (5%) (WUP-FIN, 2003).

The contributions of Tonle Sap Lake tributaries and direct rainfall into the lake are estimated at around 30% and 13%, respectively (Kummu et al., 2014). Water receding from the lake mostly flows into the Mekong River (88%) or evaporates (12%) (Kummu et al., 2014).

3. Datasets

3.1. Surface reflectances from MODIS

The MODIS spectroradiometer is part of the payload of the Aqua and Terra satellites (launched in 2002 and 1999, respectively). The MODIS sensor acquires radiances in 36 spectral bands. In this study, the MOD09A1 product (8-day binned level 3, version 6) derived from Terra raw radiance measurements were downloaded from the United States Geological Survey (USGS) Earthexplorer website (http://earthexplorer.usgs.gov). It consists in gridded surface reflectances acquired in 7 bands from 620 nm (Red) to 2155 nm (SWIR2) at a resolution of 500 m and corrected for atmospheric effect. This product is

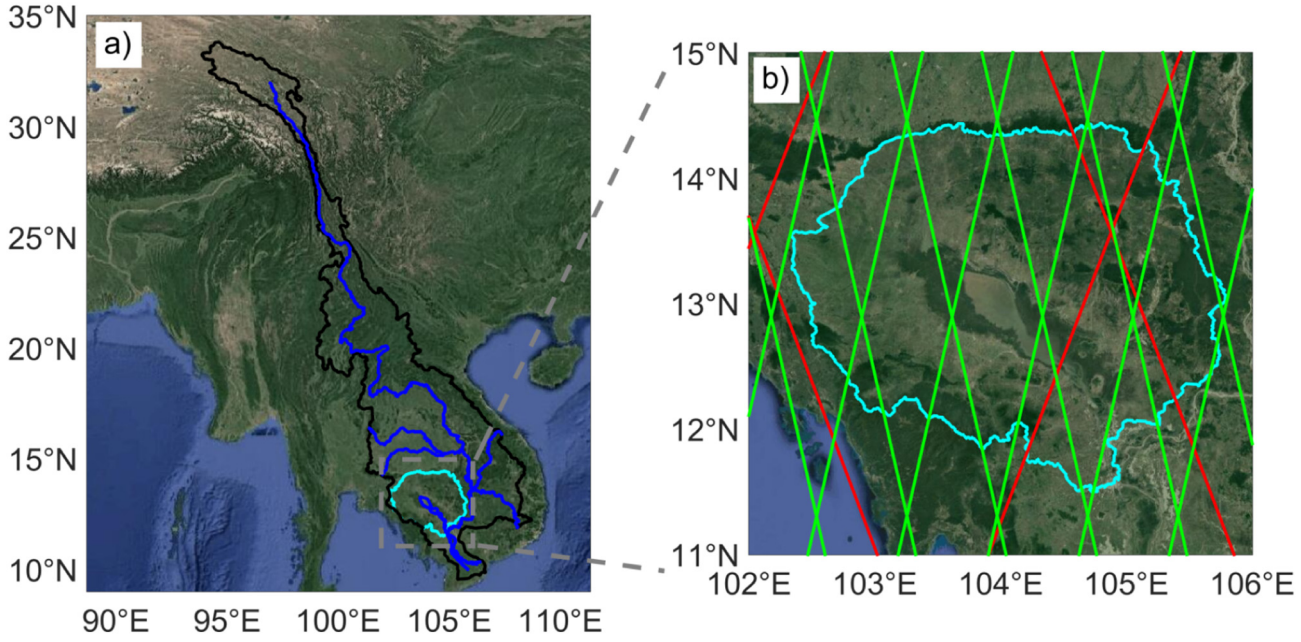

Fig. 1. a) The Tonle Sap watershed (cyan) is located in the Mekong River Basin (black), the Mekong River and its major tributaries appear in blue; b) 10-day (Jason-1, 2 and 3 in red) and 35-day (ERS-2, ENVISAT and SARAL in green) repeat period tracks over the Tonle Sap Lake watershed. Mekong River Basin boundary and drainage networkcome from the Major River Basins of the World from the Global Runoff Data Centre - Federal Institute of Hydrology (BfG) available at http://www.bafg.de/GRDC/EN/02_srvcs/22_gslrs/221_MRB/riverbasins_node.html. Tonle Sap boundaries were provided by Open Development Cambodia (http://www.opendevelopmentcambodia.net/maps/downloads/). Altimetry tracks were provided by AVISO+ (https://www.aviso.altimetry.fr/en/data/tools/pass-locator.html).
Background images come from Google Earth.

obtained by combining the best surface reflectance data of every pixel acquired during an 8-day period for each wavelength. Each MODIS tile covers an area of 1200 km by 1200 km. In this study, 815 composite images from February 2000 to December 2017 were used.

3.2. Radar altimetry data

Our radar altimetry data comes from the acquisitions on their nominal orbit of the following missions: Topex-Poseidon (1992–2002), Jason-1 (2002–2008), Jason-2 (2008–2016), Jason-3 (since 2016), ERS-2 (1995–2003), ENVISAT (2003—2010), and SARAL (2013–2016). Topex/Poseidon and Jason-1 to -3 missions are on the same 10-day repeat period orbit, whereas ERS-2, ENVISAT and SARAL succeed each other on the same 35-day repeat-period orbit. Altimetry data comes from Geophysical Data Records (GDR) E for Jason-1; GDR D for Jason-2, Jason-3 and SARAL; and GDR v2.1 for ENVISAT delivered by CNES/ESA/NASA processing centers. The data was homogenized and made available by Centre de Topographie des Océans et de l'Hydrosphère (CTOH – http://ctoh.legos.obs-mip.fr). ERS-2 data was reprocessed by CTOH to ensure continuity with ENVISAT for land studies (Frappart et al., 2016). Topex/Poseidon time series come from Frappart et al. (2006b).

3.3. Ancillary datasets

3.3.1. Water level, flood extent and volume

Our estimates were compared with the independent dataset made available by ("Impact of the Mekong River Flow Alteration on the Tonle Sap Flood Pulse," 2008) over 1997–2005 consisting of annual minima and maxima water stages, inundation extent and volume. Water stages are from the Kampong Luong station located on the lakeshore. Kummu and Sarkkula (2008) used a Digital Bathymetric Model (DBM) to established polynomial relationships between stage and extent and stage and volume. The DBM was derived from the following three spatial sources: a hydrographic survey (MRC, 1999) to determine the contours of the lake and Tonle Sap River during the dry season; a survey map (Certeza Surveying, 1964) for delineating the Tonle Sap floodplain; and the Shuttle Radar Topography Mission data ("The Shuttle Radar Topography Mission," 2007) for the surrounding areas to complete the DBM (see ("Water balance analysis for the Tonle Sap Lake-floodplain system," 2014)for more details).

3.3.2. SRTM Digital Elevation Model (DEM)

The Shuttle Radar Topography Mission (SRTM) DEM was derived from the C and X Synthetic Aperture Radar (SAR) images acquired for interferometry purposes on board the space shuttle Endeavour from 11 to 22 February 2000 (Farr et al., 2007). In this study, the SRTM 1 Arc-Second (30 m) Global elevation data was used in the Tonle Sap watershed. This dataset is available from USGS at: https://eros.usgs.gov/elevation-products.

3.3.3. TRMM/TMPA rainfall

The rainfall product used in this study is the Tropical Rainfall Measuring Mission (TRMM) Multi-Satellite Precipitation Analysis (TRMM/TMPA) 3B43 v7 product. It is a combination of monthly rainfall satellite data and other data sources at a spatial resolution of 0.25°. This dataset was derived by combining satellite information from the TRMM Microwave Imager (TMI); the Precipitation Radar (PR) and Visible and Infrared Scanner (VIRS) from the TRMM mission (operating from December 1997 to April 2015); the Special Sensor Microwave Imager (SSMI) and Special Sensor Microwave Imager/Sounder (SSMI/S) on board some satellites of the US Air Force Defense Meteorological Satellite Program (DMSP); the Advanced Microwave Scanning Radiometer – Earth Observing System (AMSR-E, operating from June 2002 to October 2011) on board Aqua satellite; Advanced Microwave Sounding Unit (AMSU) and Microwave Humidity Sounder (MHS) on board various meteorological satellites (from 1998 to now); and rain gauge observations. The TRMM 3B43v7 product merges TRMM 3B42-adjusted infrared precipitation with monthly accumulated precipitation from the Global Precipitation Climatology Center ("The TRMM Multi-Satellite Precipitation Analysis (TMPA)," Huffman et al., 2010) and is available on the Goddard

Earth Sciences Data and Information Services Center (GES DISC) website at: https://mirador.gsfc.nasa.gov/.

3.3.4. MODIS-based Global Land Cover Climatology

This climatology is based on the Collection 5.1 MODIS Land Cover Type (MCD12Q1) product at 500 m spatial resolution and obtained from analysis of MODIS images acquired between 2001 and 2010. A re-analysis attributing a confidence score for each land cover type at each pixel was performed, as substantial interannual variability in land cover types was found to affect 40% of the pixels. The final land cover classification was obtained by choosing the type with the highest confidence score between 2001 and 2010 for each pixel (Broxton et al., 2014). This dataset is available from USGS at: https://landcover.usgs.gov/global_climatology.php.

3.3.5. Climate indices

3.3.5.1. El Niño 3.4 Sea Surface Temperature index. El Niño Southern Oscillation (ENSO) oceanic indices are defined using Sea Surface Temperature (SST) anomalies in different regions of the Pacific Ocean. El Niño 3.4 SST index is computed over a region located in the eastern Pacific, between longitude 120°W and 170°W and latitude 5°N and 5°S ("Global analyses of sea surface temperature, sea ice, and night marine air temperature since the late nineteenth century," Rayner, 2003). It is available on a monthly time step starting from January 1870 at: https://www.esrl.noaa.gov/psd/gcos_wgsp/Timeseries/Nino34/.

3.3.5.2. Pacific Decadal Oscillation index. The Pacific Decadal Oscillation (PDO) index is defined as the principal component of monthly SST variability in the North Pacific, poleward of 20°N ("A Pacific Interdecadal Climate Oscillation with Impacts on Salmon Production," Mantua et al., 1997). It is available on a monthly time step starting from January 1900 at: https://www.esrl.noaa.gov/psd/gcos_wgsp/Timeseries/PDO/.

3.3.5.3. Monsoon indices. The Indian Monsoon Index (IMI) and the Western North Pacific Monsoon Index (WNPMI) are defined as the difference of 850 hPa zonal wind over the areas (5°N–15°N, 40°E–80°E) and (20°N–30°N, 70°E–90°E), (5°N–15°N, 100°E–130°E) and (20°N–30°N, 110°E–140°E), respectively, between June and September (Wang and Fan, 1999); ("Interannual Variability of the Asian Summer Monsoon," Wang et al., 2001). It is available on a yearly time step from 1948 to 2015 at: http://apdrc.soest.hawaii.edu/projects/monsoon/seasonal-monidx.html.

4. Methods

The lake and floodplain surface extent (Section 4.1) and elevation (Section 4.2) are first estimated using MODIS and radar altimetry measurements, respectively. They are then combined to compute the lake storage change (Section 4.3). Finally, a rainfall standardized anomaly index is computed (Section 4.4) to investigate the link between this storage change and rainfall.

4.1. Surface water extent

The approach developed by (Sakamoto et al., 2007) and simplified by Normandin et al. (2018) to monitor flood extent in the Mekong Basin was applied to the Tonle Sap drainage area (processing steps are presented in Fig. S1 in the Supplementary material section). It is based on the thresholding of the Enhanced Vegetation Index (EVI), the Land Surface Water Index (LSWI), and the Difference Value between EVI and LSWI (DVEL) to determine the status (non-flooded, mixture, flooded, permanent water body) of any pixel in an 8-day composite MODIS image of surface reflectance. These two spectral indexes were selected as the Short-wave infrared (SWIR) band is very sensitive to soil and vegetation moisture content and because the Near infrared (NIR) band presents low surface reflectance values over water bodies and high values over densely vegetated areas, whereas surface reflectance values in the red band are higher for vegetation than over water bodies. Thus, these two indexes are well suited to discriminate between water and vegetation.

The two indexes used in this approach are defined as follows (Huete, 1997):

$$EVI = 2.5 \times \frac{\rho_{NIR} - \rho_R}{\rho_{NIR} + 6 \times \rho_R - 7.5 \times \rho_B + 1} \quad (1)$$

$$LSWI = \frac{\rho_{NIR} - \rho_{SWIR}}{\rho_{NIR} + \rho_{SWIR}} \quad (2)$$

where ρ_{NIR} is the surface reflectance value in the near infrared (841–875 nm, band 2), ρ_R is the surface reflectance value in the red (621–670 nm, band 1), ρ_B the surface reflectance value in the blue (459–479 nm, band 3), and ρ_{SWIR} the surface reflectance in the short-wave infrared (1628–1652 nm, band 6).

Following (Sakamoto et al., 2007), the approach summarized in Fig. S1 for Normandin et al. (2018) was applied to the series of MODIS images. First, the pixels identified as cloud-covered were filtered out ($\rho_B \geq 0.2$). Then, a linear interpolation was performed to limit information loss over the study area. The pixels are classified into two major classes: non-flooded (EVI > 0.3 or EVI ≤ 0.3 but EVI – LSWI > 0.05) and water-related pixels (EVI ≤ 0.3 and EVI – LSWI ≤ 0.05 or EVI ≤ 0.05 and LSWI ≤ 0). This latter class is divided into 3 sub-classes: mixture pixels when 0.1 < EVI ≤ 0.3, flooded pixels EVI ≤ 0.1, and long-term water bodies (e.g., rivers and lakes) when a pixel is determined flooded >250 days per year. Spatio-temporal variations of the flood were determined in the Tonle Sap drainage basin from February 2000 to December 2017.

4.2. Altimetry-based water levels

4.2.1. Post-processing of altimeter data

Radar altimetry was initially developed to provide accurate measurements of the sea surface topography and is now commonly used for the monitoring of inland water levels (see (Crétaux et al., 2017) 2017 for a recent review). Variations of altimeter height from one cycle to another can be associated with water level changes.

In this study, we used the Multi-mission Altimetry Processing Software (MAPS) for processing altimetry data over land and ocean (e.g., Frappart et al., 2015a,c; Biancamaria et al., 2017; Vu et al., 2018), that allows to build time-series of water levels at a virtual station (intersection between satellite track and water body), after a refined selection of the valid altimeter data. Data processing is composed of four main steps:

i) a rough delineation of the cross-section between the altimeter tracks and Tonle Sap using Google Earth (Fig. 1b);
ii) loading of the altimetry over the study area and computation of altimeter heights from raw data contained in the GDR;
iii) a refined selection of the valid altimetry data through visual inspection;
iv) computation of the water level time-series as the median of the selected water levels for each cycle.

A detailed description of altimetry data processing using MAPS can be found in (Frappart et al., 2015b). MAPS is available via CTOH. Previous studies have shown that Ice-1-derived altimetry heights are the most suitable for hydrological studies in terms of water level accuracy and data availability (e.g., (Frappart et al., 2006a,b; (Santos da Silva et al., 2010). They are among the commonly available retracked data in the GDR.

Measurement bias between missions and difference in satellite track locations were computed and removed from each time series to obtain a

consistent time series over the lake between all missions. The final water elevation time series (in meters wrt EGM08 geoid) is computed with reference to ENVISAT track 107 (the most eastward ENVISAT track on the lake, see Fig. 1b).

4.2.2. Specific processing of Topex-Poseidon and Jason time series

As shown in Fig. 1b, Topex-Poseidon and Jason track over Tonle Sap Lake is very close to its outlet. Consequently, and as visually observed on Landsat images, during low flow period the observed area is representative of the Tonle Sap River, which connects the lake to the Mekong River, whereas during high flow period it fully includes the lake extent. Correlation between Jason-2 time series and ENVISAT over the period in common (>2 years) still remains high (0.9936), with an RMSE of 0.23 m, after removing the common bias between the two time series. For low water elevations (below 5.5 m), Jason-2 water elevations rise before those of ENVISAT and decrease later. This could be due to hydraulic effects: water elevations vary differently in the lake and outlet river because of bathymetry changes. To account for this observation in a simple way, we arbitrarily considered that difference between the two time series can be corrected applying a time lag to Jason-2 time series, depending on the water elevations, to get a better match with ENVISAT time series. After different tests on time lags and water elevation thresholds, the best correlation (0.9986) and lowest RMSE between ENVISAT and Jason-2 (0.11 m) are obtained when Jason-2 water elevations below 5.5 m are delayed by 9 days, whereas water elevations above this threshold are delayed by 2 days. More information on this issue is shown in Figs. S2 to S4 in the Supplementary information section. The Topex-Poseidon, Jason-1 and Jason-3 time series used in this study are from the same track and therefore the same processing has been applied (after removing the bias between these time series and Jason-2 time series).

4.3. Surface water volume variations

MODIS-based flood extents were combined with altimetry-derived water levels to estimate lake volume variations. Due to the extent of flooding in the watershed, our analysis was limited to the pixels which are i) under water filling SRTM DEM with the water stage of the lake (see the supplementary information, Section 2, for method) and ii) connected to the lake using a four-connected neighborhood. As flood extent is derived from a shorter time period than water stage (1993–2017 instead of 2000–2017), a polynomial relationship between water stage (h) and lake surface (S) was fitted to estimate surface water extent during the whole altimetry period using Eq. 3:

$$S(h) = \sum_{i=1}^{n} a_i h^i \quad (3)$$

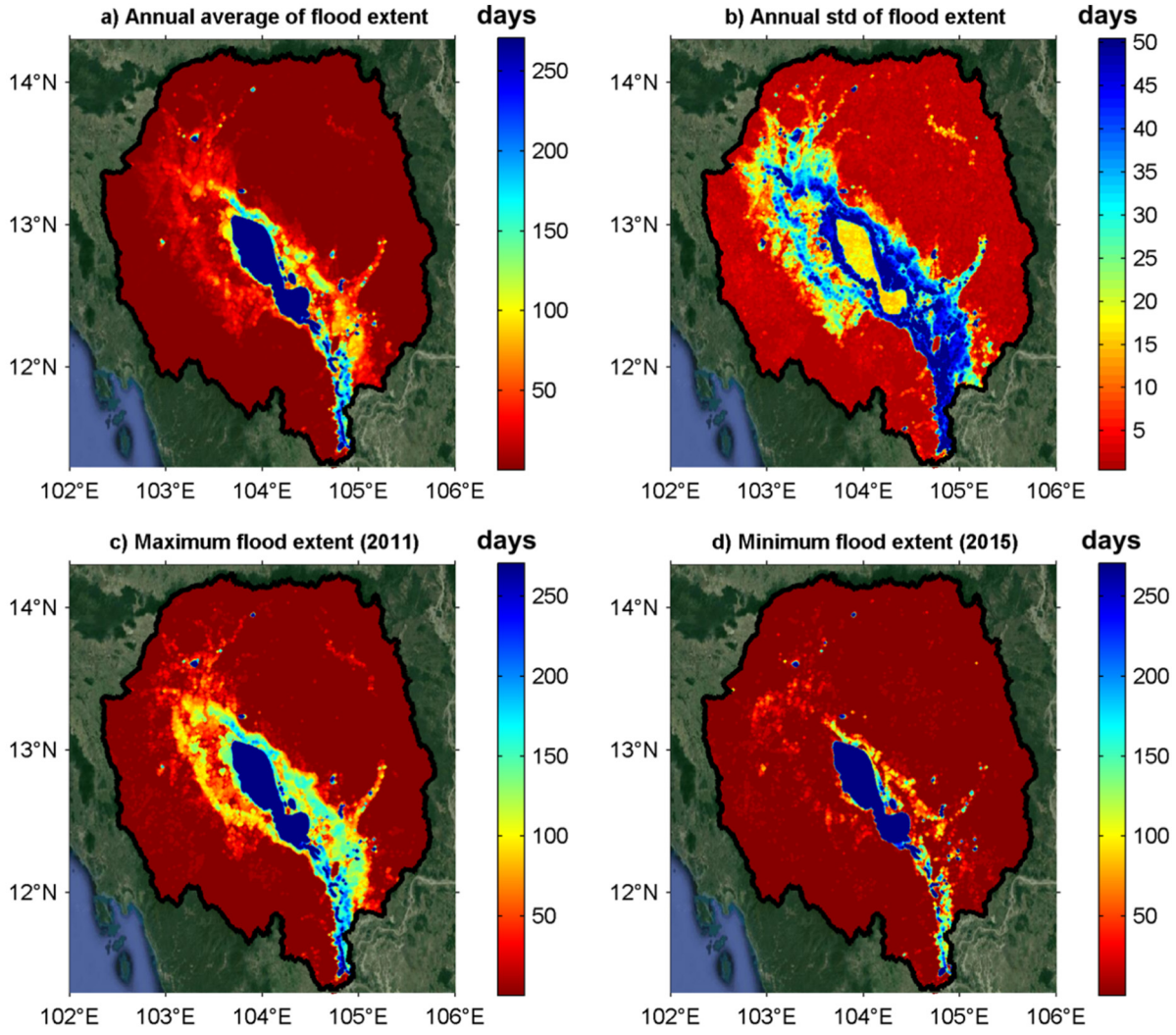

Fig. 2. a) Maps of annual flood duration averaged over 2000/2017 time period and b) associated standard deviations expressed in days, using only pixels classified as "inundated". c) Maps of flood duration in 2011 (year with the maximum flood extent over the whole time period) and d) in 2015 (year with the minimum flood extent), considering only pixels classified as inundated. Background images come from Google Earth.

where a_i is the coefficient of degree i of the polynomial and n the maximum degree of the polynomial. A confidence interval of 95%, a RSME of 74 km^2 and R^2 of 0.99 were found using a second degree polynomial with the following values: $a_0 = 6013.0$ km^2, $a_1 = -1518.0$ km and $a_2 = -176.9$. As in Baup et al. (2014) or Crétaux et al. (2015, 2016), the volume variations of the lake (ΔV), between two consecutive time steps ($t-1$ and t) were estimated using the assumption of a regular morphology of the lake and a pyramidal shape:

$$\Delta V = \frac{(h(t)-h(t-1)\left(S(t)+S(t-1)+\sqrt{S(t)S(t-1)}\right)}{3} \quad (4)$$

4.4. Standardized Precipitation Anomaly Index

The Standardized Precipitation Anomaly Index (SPAI) was defined by (Lamb, 1982) to study interannual rainfall variations:

$$I_R(t) = \frac{1}{n}\sum_{i=1}^{n}\frac{R(i,t)-\langle R(i,\tau)\rangle_{\tau\in T}}{\sigma(R(i,\tau))_{\tau\in T}} \quad (5)$$

where $R(i,t)$ is the annual rainfall at TRMM 3B43v7 gridpoint i for hydrological year t, $\langle R(i,\tau)\rangle_{\tau\in T}$ and $\sigma(R(i,\tau))_{t\in T}$ are the annual average and standard deviation over the reference period T at gridpoint i, respectively, and n is the total number of gridpoints in the study area. The hydrological year is defined between November of year $t-1$ and October of year t.

5. Results and discussion

5.1. Validation of surface water extent and storage

Variations of lake surface extent were estimated between February 2000 and December 2017 by applying the threshold approach to MODIS images. The average number of days per year with missing data due to cloud presence was computed for each pixel, as well as the associated standard deviation over the whole study period (see Fig. S5 in Supplementary information). The annual lack of data due to cloud presence over Tonle Sap Lake and its floodplains is generally <8 days (1 image) and can reach up to 24 days (3 images), with standard deviations <16 days (2 images). This lack of data (not occurring on consecutive dates) does not prevent the use of MODIS images for monitoring Tonle Sap seasonal flooding. Maps of annual average duration of inundation extent and associated standard deviation are presented in Fig. 2a and b, respectively, along with maximum and minimum inundation extents during the flood peak in 2011 (Fig. 2c) and 2015 (Fig. 2d), respectively, considering only pixels classified as inundated. Fig. 3 is similar to Fig. 2, but uses both pixels classified as inundated and the ones classified as mixed pixel. Extensive inundation is generally in the western part of the lake during time spans shorter

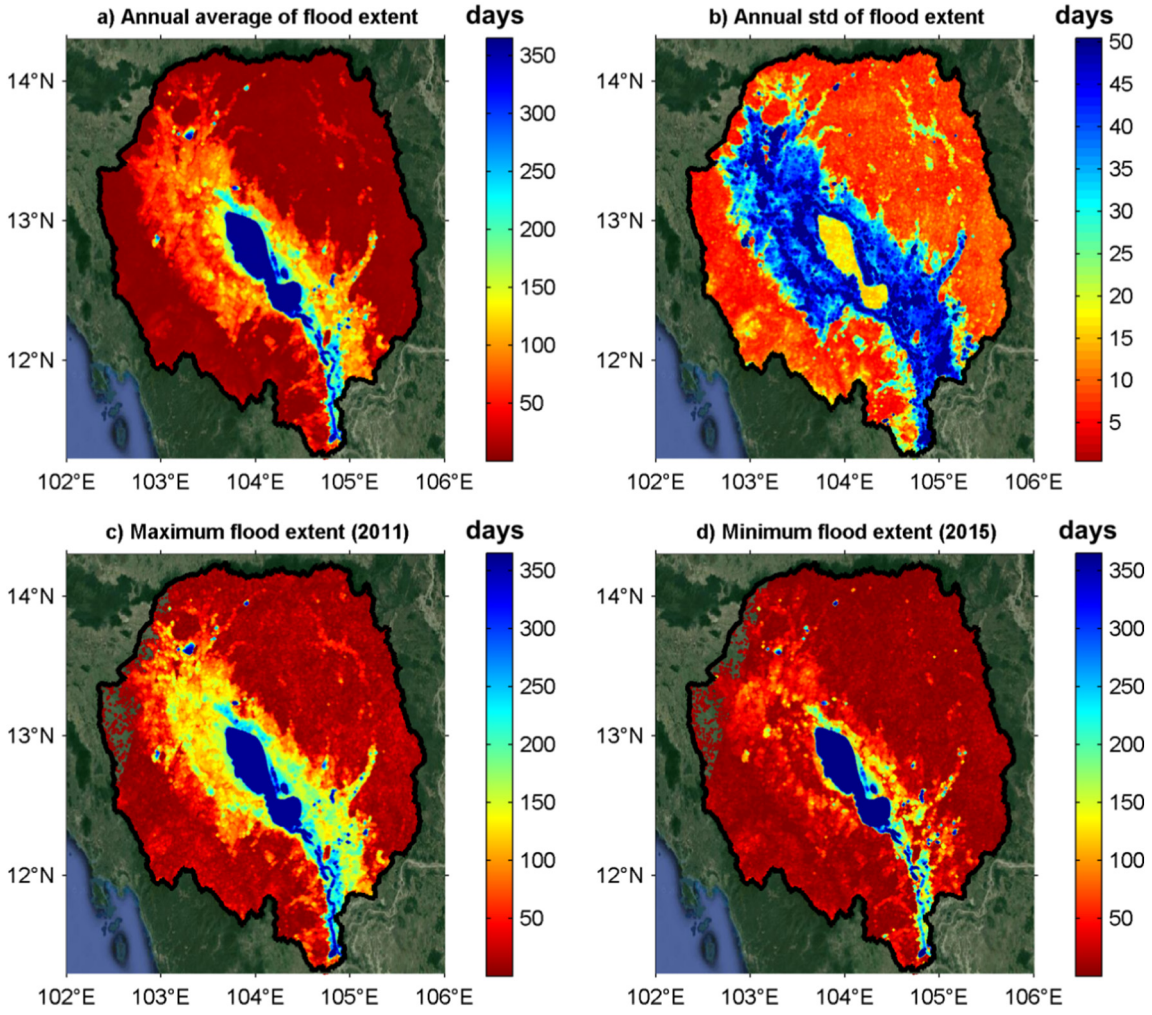

Fig. 3. a) Maps of annual flood duration averaged over 2000/2017 time period and b) associated standard deviations expressed in days, using pixels classified as "inundated" and pixels classified as "mixed pixels". c) Maps of flood duration in 2011 (year with the maximum flood extent) and d) in 2015 (year with the minimum flood extent), considering inundated and mixed pixels. Background images come from Google Earth.

than 3 months, but can also occur in the eastern part of the lake and along its north to south flowing tributary in the eastern part of the basin. Longer inundation, lasting between 4 and 5 months but of smaller extent, can be observed in the lake's outlet and also in the northeastern part (Fig. 2a). These inundations are characterized by a large interannual variability with standard deviations between 40 and 50 days (Fig. 2b). In 2011, important inundations (>100 days) were observed in all eastern and northwestern parts of the lake (Fig. 2c), whereas almost no flooding was detected in 2015 (Fig. 2d). In addition, considering the mixed pixels (i.e., the pixels partly inundated), the patterns are similar to those presented in Fig. 2, but with a larger extent and longer presence (Fig. 3). Floods lasting up to 6 months were detected in the western parts of the lake (Fig. 3a and c), and are in good agreement with results from previous studies (Kummu and Sarkkula, 2008; Arias et al., 2012; Kummu et al., 2014). Large differences were obtained between the flood extent using only the flooded pixels and using both the flooded and mixed pixels in terms of maximum extent and flood duration inside the maximum inundation extent defined filling SRTM DEM with altimetry-based water stage (Fig. S6). Even if SRTM DEM exhibits a high frequency noise (variations of 1 or 2 m from one pixel to another, see Fig. S7), large-scale elevation variations are well retrieved considering the minimum elevation in the MODIS pixels (Fig. S8) and do not

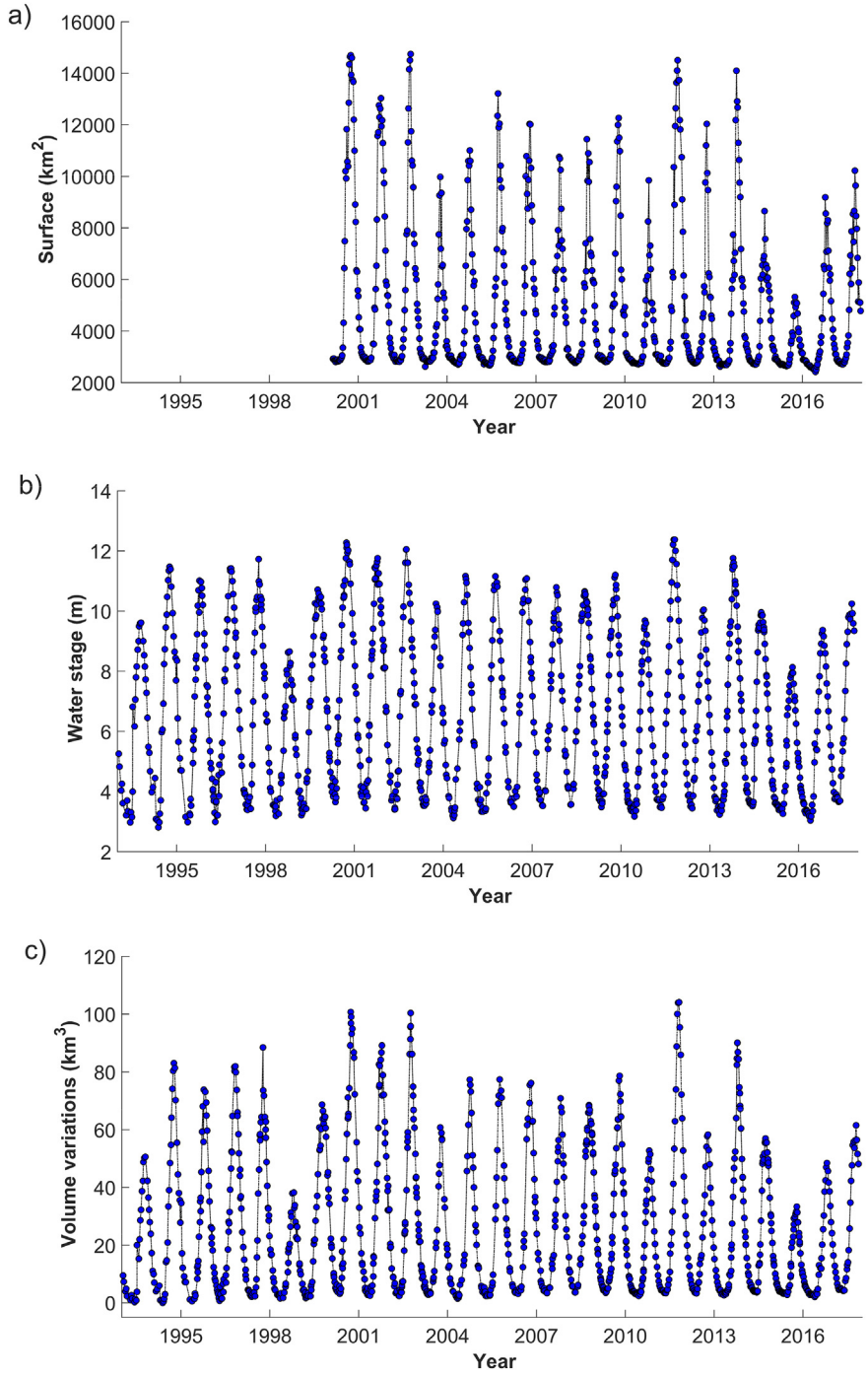

Fig. 4. Time series of a) surface water extent (in km^2) in the Tonle Sap basin based on the processing of MODIS images, over 2000–2017, b) altimetry-based water level of the Tonle Sap Lake (in m wrt EGM08 geoid), combining information from Topex/Poseidon (1993–2002), ERS-2 (1995–2003), Jason-1 (2002–2008), ENVISAT (2003–2010), Jason-2 (2008–2016), SARAL (2013–2016) and Jason-3 (since 2016), c) water volume variations of the Tonle Sap lake obtained applying the surface-height relationship over 1993–2017.

prevent its use for determining temporal variations of maximum flood extent. In the following, surface water extents were obtained by considering both the flooded and mixed pixels which are i) under water filling SRTM DEM with the water stage of the lake and ii) connected to the lake using a four-connected neighborhood.

Fig. 4a presents temporal variations of surface water extent in the Tonle Sap drainage basin between February 2000 and December 2017 using MODIS images. They exhibit a well-marked seasonal cycle, with minima occurring in April and May and maxima between September and November. There is a strong interannual variability of the maximum flood extent ranging from 5114 km^2 in October 2015 up to 13,736 km^2 in October 2011. The minimum lake surface varies between 2320 km^2 in 2016 and 2800 km^2 in 2000 during low stage. Water stage changes accordingly, with an annual amplitude (i.e. difference between the maximum and the minimum over the year) varying from 5.5 m in 2015 to 9 m in 2011 (Fig. 4b), resulting in volume variations of Tonle Sap lake that range from 31 km^3 in 2015 to 101 km^3 in October 2000 and 2011 (Fig. 4c). Comparisons were made using annual amplitude of the lake water stage, inundated surface in the Tonle Sap basin, and water volume estimated by Kummu and Sarkkula (2008) using a Digital Bathymetric Model (DBM) and in situ water levels, over the common period of availability of the different datasets (i.e., 1997–2005 for water stages and volumes, and 2000–2005 for inundated surfaces). A very good agreement was found (in terms of annual amplitude) between altimetry-based and in situ water levels ($R = 0.97$, RMSE = 0.27 m and RRMSE = 3.5%), and multi-satellite-derived and Kummu and Sarkkula (2008) water volume variations ($R = 0.96$, RMSE = 12 km^3 and RRMSE = 19%). A good agreement was also found between MODIS-based and Kummu and Sarkkula (2008) surface water extent ($R = 0.89$, RMSE = 982 km^2 and RRMSE = 9.9%). If the very good agreement between in situ and altimetry-based water levels can confirm observations from Topex/Poseidon in a previous study with a RMSE of 0.23 cm (Frappart et al., 2006b), the small discrepancies observed in surface water extent and volume can be attributed to differences of approach in Kummu and Sarkkula (2008) and our own study. The composite DBM including old measurements of the floodplain's topography is liable to introduce some errors to Kummu and Sarkkula's (2008) approach, whereas the delineation of inundation extent using images at the moderate resolution of 500 m and the SRTM DEM is responsible for overestimation of the flooded area due to the presence of mixed pixels. Nevertheless, both approaches present very consistent results and can be used to estimate water balance in the drainage area.

Over the study period, interannual variations of surface water volume were computed from monthly lake water volume with the removal of monthly climatological averages. The range is between −35.99 km^3 in 2015 to 35.53 km^3 in 2000 (Fig. 5a). The variations were compared with SPAI (see Section 4.4) from TRMM/TMPA 3B43 averaged over the Tonle Sap watershed and over the entire Mekong Basin from 1998 to 2017 (Fig. 5b). Correlation coefficients between the interannual variations of surface water volume and SPAI (defined during the hydrological year between November of year $n-1$ and October of year n) are equal to 0.61 (p-value = $5.1.10^{-3}$) and 0.77 (p-value = 10^{-4}) for the Tonle Sap watershed and the Mekong Basin, respectively. These results are related to the hydrological regime of the Tonle Sap watershed, whose flood pulse is driven by the flow of the Mekong River. Annual precipitation anomalies can account for the large droughts of 1998, 2010 and 2015 and large floods of 2000, 2001 and 2011 with SPAI lower than −1 and higher than 1, respectively, for both the Tonle Sap watershed and the Mekong Basin, but cannot explain the large flood of 2002 and large drought of 2016 according to TRMM/TMPA 3B43 dataset. Similar comparisons were performed during the dry and rainy seasons. Correlation coefficients were found equal to 0.31 (p-value = 0.19) and 0.84 (p-value close to 0) during the dry and rainy seasons, respectively, for the Mekong Basin and to 0.45 (p-value = $4.5.10^{-2}$) and 0.58 (p-value = $7.5.10^{-3}$) during the dry and rainy seasons, respectively, for the Tonle Sap watershed. These results confirm that surface water volume of the Tonle Sap watershed is strongly influenced by rainfall during the rainy seasons in the Mekong Basin. During the large flood events of 2000, 2001 and 2011, SPAI during the rainy season of between 1 and 1.5 were obtained in the whole Mekong Basin (Fig. 5c). Larger floods were recorded in 2000 and 2011 as they were enhanced by SPAI between 1 and 1.5 in the Tonle Sap watershed. A very low positive SPAI was observed in the Tonle Sap watershed during the wet season of 2001. However, high positive anomalies (~2) were observed in the dry season and contributed to the excess in surface water storage for the same year (see Fig. 5d). This was also observed in the year 2000,

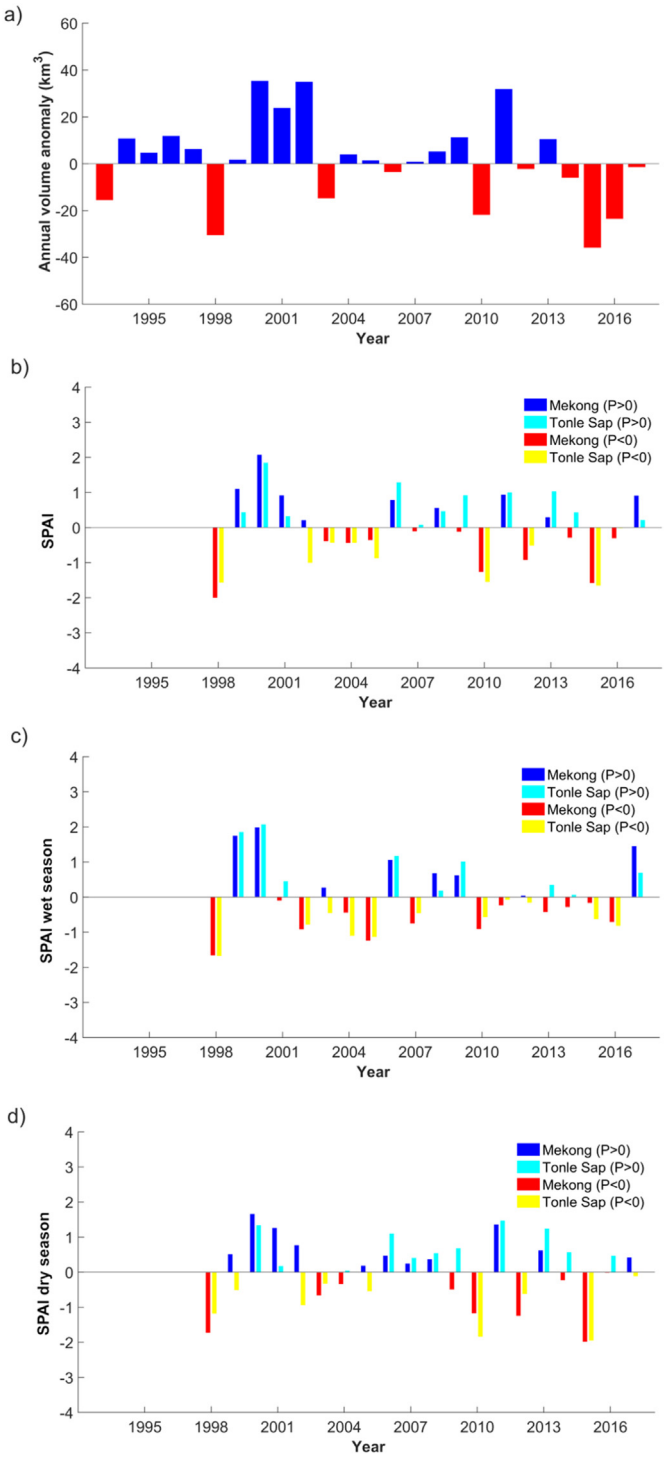

Fig. 5. a) Interannual variations of annual surface water storage. b) Annual, c) dry and d) wet seasons SPAI in the Mekong Basin and in the Tonle Sap watershed.

which was the largest flood between 1995 and 2016. Inverse conclusions can be made for the large droughts of 1998, 2010 and 2015 with SPAI between −1.5 and −2 (Fig. 5c) during the wet season. Lower rainfall during the dry season seems to have a low impact as small anomalies were observed during the lowest drought in 2015 (Fig. 5d). The 2002 flood was higher than that of 2001 in spite of a much lower positive SPAI. This was due to a higher than usual lake level at the beginning of the 2002 hydrological year. Conversely, low rainfall deficit was responsible for low water surface storage in 2016 due to the very low lake level at the end of the 2015 hydrological year. For a comparison, the anomaly of lake water volume was 6.8 km^3 in December 2001 and −21.9 km^3 in December 2015. In addition, daily in-situ data of water levels recorded at the Prek Kdam station in the Tonle Sap River (which joins the Mekong River to Tonle Sap Lake) are displayed on the Mekong River Commission website during both dry and flood seasons since 2013 (ffw.mrcmekong.org/historical_rec.htm). A visual inspection showed very similar water stage amplitude between in situ and altimetry time series. Extreme events were defined by considering deviations larger (lower) than two thirds of the maximum (minimum) estimated over the observation period (i.e., around ±24 km^3). Four positive and three negative extrema can be observed. For positive extrema: between July and November 2000, peaking at 36.36 km^3 in September 2000; 24.22 km^3 in September 2001; in September and October 2002, peaking at 35.37 km^3 in September 2002; and in September and October 2011, peaking at 30.77 km^3 in October 2011. For negative extrema: between September and November 1998, peaking at −31.42 km^3 in October 1998; between September and November 2015, peaking at −36.07 km^3 in October 2015; and −24.22 km^3 in September 2011 (Fig. 6a). In the following, we compare these exceptional droughts and floods to climatic indexes to see if they are related to climate variability.

5.2. Surface water storage and climate variability

Positive anomalies of surface water volume in the Tonle Sap watershed in September–October correspond to negative values of ENSO3.4 index defined by Rayner (2003) (Fig. 6b). On the contrary, negative anomalies of surface water volume in the watershed correspond to positive values of ENSO 3.4. Larger anomalies occur when ENSO index and the Pacific Decadal Oscillation (PDO) index (as defined by Mantua et al. (1997)) exhibit large deviations and are in phase. Large positive (respectively negative) anomalies of the lake volume are obtained for moderate (between 1 and 1.5 °C) to very strong (above 2 °C) negative (respectively positive) values of both ENSO (El Niño, respectively La

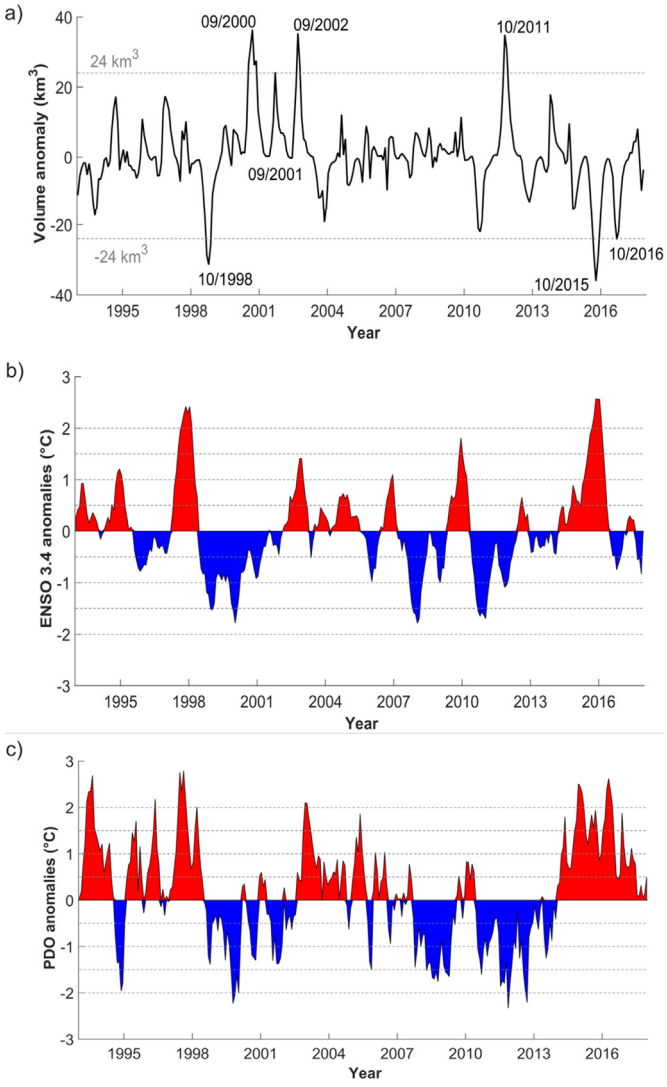

Fig. 6. Interannual variations of monthly a) surface water volume of the Tonle Sap watershed, b) anomalies of ENSO 3.4 and c) PDO indices over 1993–2017.

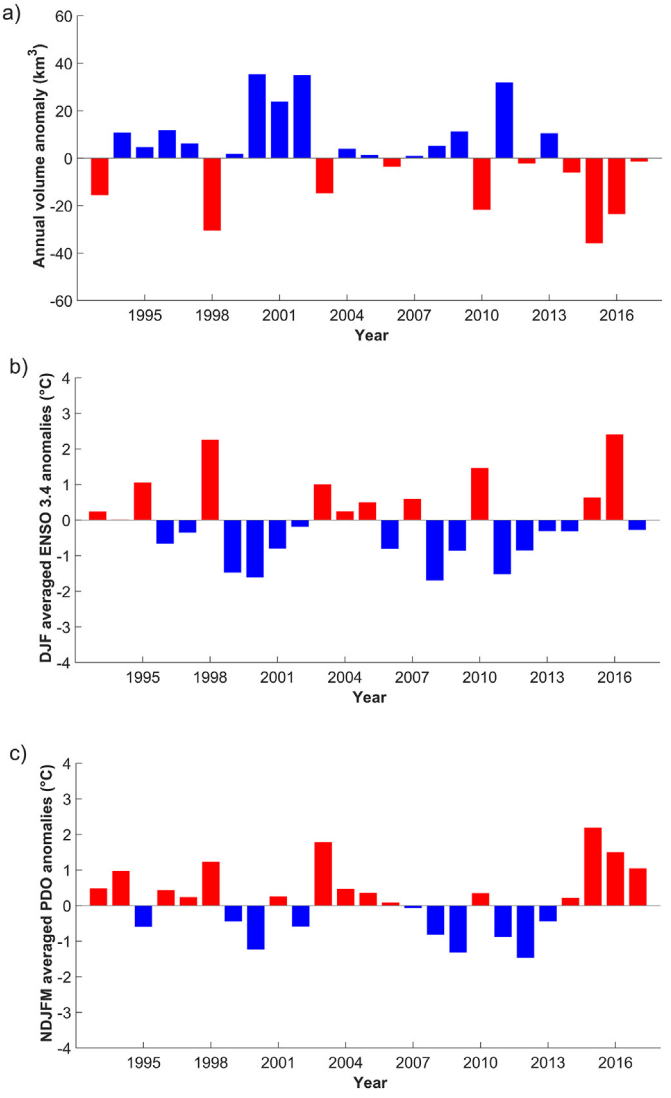

Fig. 7. Interannual variations of annual a) surface water storage between 1993 and 2017, b) anomalies of ENSO 3.4 averaged over December to February (DJF) and c) PDO averaged over November to March (NDJF).

Niña, Fig. 6b) and PDO (Fig. 6c) during the previous winter. This phenomenon is caused by a significant intensification of the negative relationship between ENSO and the monsoon when ENSO and PDO are in phase. It was previously described regarding the East Asian monsoon (Kim et al., 2014). Positive values of ENSO and PDO are associated with anomalous warm temperature patterns over East Asia that cause rainfall deficit the following summer. Negative values of ENSO and PDO are linked with anomalous cold temperature patterns, leading to excess rainfall the following summer. On the contrary, when ENSO and PDO are out of phase, interannual variations are lower. The super strong ENSO event in 2015/2016 was an exception, as it did not result in huge rainfall in either the Tonle Sap watershed or the Mekong

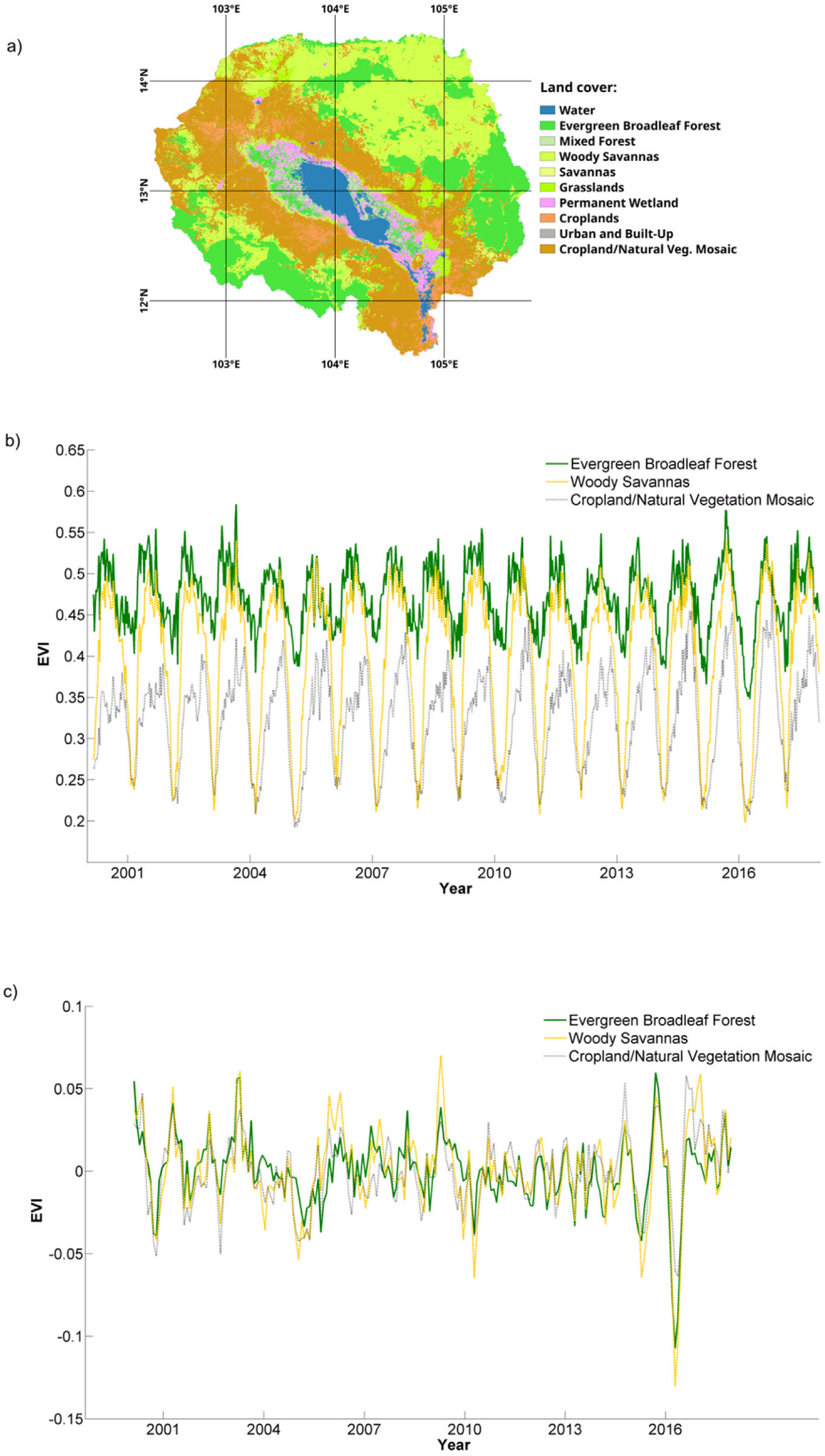

Fig. 8. a) Land cover map of the Tonle Sap watershed from the 500 m MODIS-based Global Land Cover Climatology, b) time series of EVI and c) EVI interannual anomaly averaged over Evergreen Broadleaf Forest (green), Woody Savannas (orange) and Cropland/Natural Vegetation Mosaic (black).

Basin. This was most likely due to its rapid decay in boreal spring 2016 causing a weakening of the western Pacific subtropical anticyclone (Liu et al., 2017). Correlation between annual amplitude of volume variations and climatic indices were also estimated, and several time-periods were tested. Stronger correlations were found when the ENSO index was averaged over December to February (DJF) as in Räsänen and Kummu (2013) and when the PDO index was averaged over November to March (NDJFM) as in Newman et al. (2003). For $ENSO_{DJF}$, R = −0.70 with a p-value equal to 10^{-4}, whereas for PDO_{NDJFM}, R = −0.68 with a p-value equal to 2.10^{-4}. This confirms earlier findings about relationships in the Mekong Basin between rainfall, discharge, ENSO (Räsänen and Kummu, 2013) and PDO (Delgado et al., 2012). An even higher correlation was found between annual anomalies of surface water storage and ENSO 3.4 index than between annual flow and ENSO 3.4 (Räsänen and Kummu, 2013) and this study provides a quantification of the relationship between flood pulse and PDO in the Mekong Basin. The optimal least-squares linear combination of both indices provides a correlation of −0.75. The coefficients of this linear combination are equal to 1.0 and 0.84 for ENSO 3.4 and PDO, respectively. Time series of annual amplitude of lake volume (Fig. 7a), of the ENSO 3.4 index averaged over DJF (Fig. 7b) and of the PDO index averaged over NDJFM (Fig. 7c) illustrate differences in the impact of extreme events on lake volume. The drought of 1998 and the floods of 2000 and 2011 are directly related to large positive and negative anomalies of both ENSO 3.4 and PDO. The 2002 flood and 2015/2016 droughts can be attributed to both a large value in module of either ENSO 3.4 or PDO (and a lower value of the other index), and the existence of an excess (since 2000) or a deficit (since 2014) of water in the lake. This shows that the possibility of occurrence of a hydrological extreme is not only conditioned by climate factors but also by base water storage from previous years.

We propose to quantify the monsoonal impact on lake storage, as the flood pulse in the Mekong Basin is driven by the monsoon. The Mekong Basin is under the influence of both the Indian and the Western North Pacific Monsoons (Delgado et al., 2012). Correlation between anomalies of annual surface water storage and Western North Pacific Monsoons (WNPMI, Wang et al., 2001) and Indian Monsoon (IMI, Wang and Fan, 1999) provides better results (R = 0.55, p-value = 0.006, and R = 0.49, p-value = 0.018) for July and August, respectively. This is similar to the relationship between water discharge and WNPMI in the downstream Mekong Basin discovered by Delgado et al. (2012).

5.3. Impact of the 2015 extreme drought on vegetation activity

Vegetation activity is highly related to flood duration (Arias et al., 2013). In the following, impact of the 2015 drought on the Tonle Sap ecosystem is analyzed using MODIS-derived EVI time series and a land cover map. The 1998 and 2015 extreme droughts were the worst observed during the study period, but MODIS images are only available since February 2000. Due to this, our analysis is limited to the 2015 drought. Fig. 8a shows land cover types from the 500 m MODIS-based Global Land Cover Climatology (Broxton et al., 2014) for the Tonle Sap Basin. Time series of Enhanced Vegetation Index (EVI) and their interannual variations (estimated by removing the climatological monthly mean to the monthly values) were computed for each land cover type. In the following, only land cover types corresponding to vegetation are considered. They are presented for the three main land cover types which cover 80.3% o of the Tonle Sap basin surface (Evergreen Broadleaf Forest, Woody Savannas and Cropland/Natural Vegetation Mosaic) as seen in Fig. 8b and c for the time series and associated anomalies, respectively, and in Fig. S9a and b for the five other classes of vegetation which cover 14.6% of the surface of the Tonle Sap Basin surface (Mixed Forests, Savannas, Grasslands, Permanent Wetlands and Croplands). Lower than usual minimum values of EVI are observed in spring 2016 for all land cover types as shown in Figs. 8b and S9a. The anomalies reached their lowest values in April 2016 for Evergreen Broadleaf Forest, Woody Savannas and Cropland/Natural Vegetation Mosaic with EVI anomalies of −0.11, −0.13 and −0.06 (Fig. 8c), corresponding to an annual variation of amplitude around 0.10, 0.25 and 0.15, respectively. The same timing is observed for Savannas, Grasslands and Permanent Wetland with EVI anomalies of −0.10, −0.05 and −0.12 (Fig. S9b), corresponding to an annual variation of amplitude around 0.25, 0.10 and 0.30, respectively. They reached their lowest values in May 2016 for Mixed Forests and Croplands with EVI anomalies of −0.15 and −0.04 (Fig. S9b), corresponding to annual variation of amplitude around 0.10 and 0.15, respectively. The spatial distribution of anomalies of EVI for April and May are presented in Fig. 9a and b, respectively. They are quite similar to lowest anomaly values in April 2016. The largest negative anomalies are located on the Woody Savannas in the northeast and southwest of the watershed, as well as on the Evergreen Broadleaf Forest located in the east and southwest, and the grasslands of the downstream part. Croplands were generally less affected thanks to irrigation. Some rare positive anomalies were also found around the lake. For instance, the extreme drought of 2015 modified vegetation activity during the first semester of 2016. The temporal evolution of EVI of the Evergreen Broadleaf Forest, Woody Savannas and Cropland/Natural Vegetation Mosaic (Fig. 10) as well as Savannas, Grasslands and Croplands (Fig. S10) exhibit a longer and lower than usual period of low activity (until June instead of April) where it presents minimum activity between January and June instead of a maximum for Mixed Forests and Wetlands (Fig. S10). Normal and even slightly above normal EVI values are found for the rest of 2016 and also for 2017 (Figs. 8b, c, S9a and S9b).

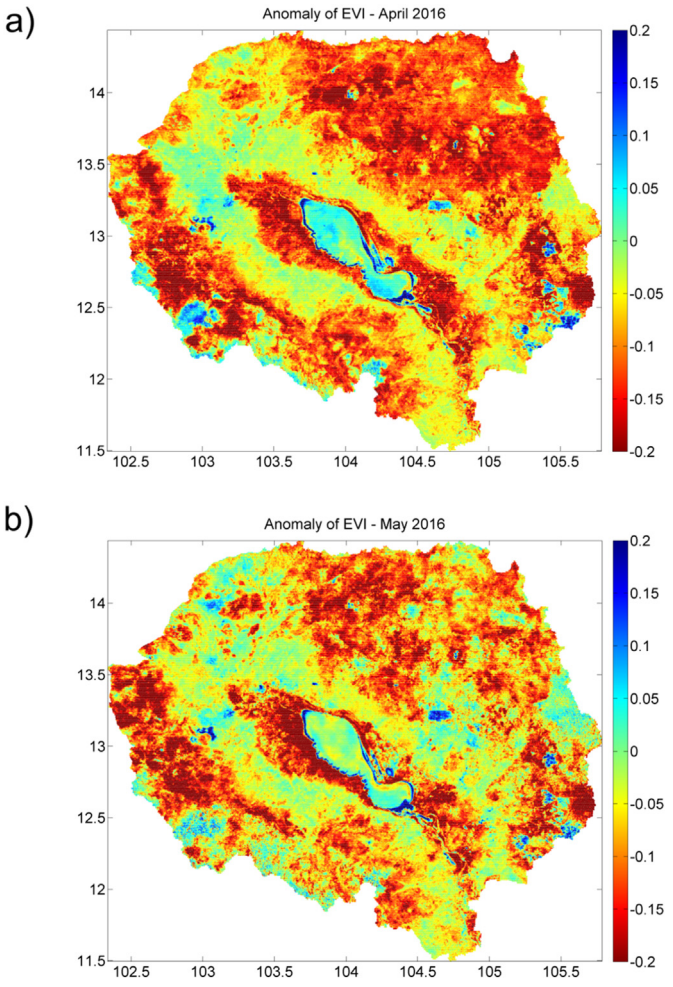

Fig. 9. Anomaly maps of EVI over the Tonle Sap watershed for a) April and b) May (b) 2016.

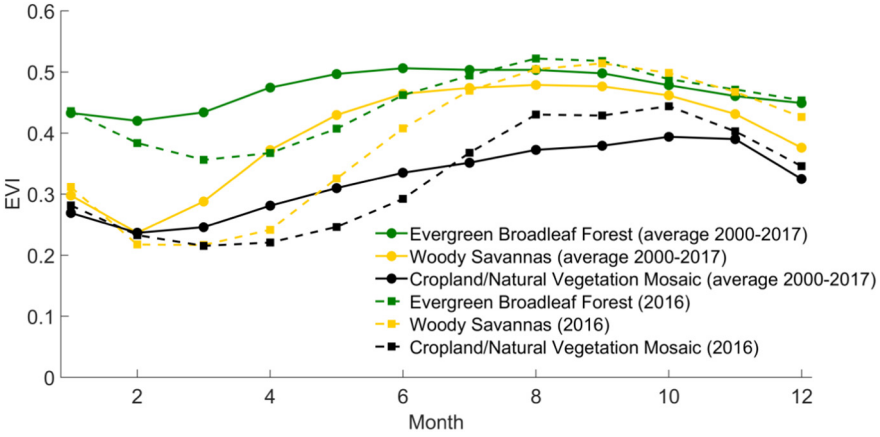

Fig. 10. Monthly variations of EVI averaged over 2000–2017 (continuous line) and EVI for 2016 (dotted line) for the Evergreen Broadleaf Forest (green), Woody Savannas (orange) and Cropland/Natural Vegetation Mosaic (black).

6. Conclusion

Surface water storage variations of Tonle Sap were determined combining remotely sensed inundation extent data derived from MODIS reflectance images and altimetry-based water levels from 1993 to 2017. Their interannual anomalies were found to be more related to the rainfall occurring in the Mekong Basin ($R = 0.77$ for the interannual variations during the whole hydrological year) than in the Tonle Sap watershed ($R = 0.61$) as flooding in the Tonle Sap watershed is mostly driven by the flow of Mekong River. Nevertheless, extreme events (exceptional floods and droughts) occurred when large excess/deficit rainfall occurred during the rainy season in both the Mekong Basin ($R = 0.84$) and Tonle Sap watershed ($R = 0.58$). Excess rainfall occurring in both dry and rainy seasons in the Mekong Basin combined with a rainfall deficit in the Tonle Sap watershed during the rainy season was only seen to cause large flooding in 2001. Important memory effects were also detected as in the extreme flood of 2002. This was mostly due to excess in surface water storage of the exceptional flood of 2000 and the large flood in 2001, whereas the extreme drought of 2016 was caused by the deficit in surface water by the drought of 2014 and the extreme drought of 2015. A quasi-equal influence of the West North Pacific and Indian Monsoons was also found with correlations between the interannual variations of surface water storage and the WNPMI in July of 0.55 and the IMI in August of 0.49.

Interannual variations of surface water storage in the Tonle Sap watershed are strongly influenced by climate variability. They exhibit large positive and negative anomalies corresponding to extreme drought (1998, 2015, and 2016) and flood (2000, 2001, 2002, and 2011) events. They were related to the very strong El Niño events of 1997–1998 and 2015–2016 and the moderate La Niña events of 1999–2000 and 2010–2011 enhanced by the PDO. Correlation coefficients between the interannual variations of surface water storage of the Tonle Sap watershed and the average ENSO 3.4 index over DJF and PDO over NDJFM were found equal to −0.70 and −0.68, respectively. R of −0.75 was found using a linear combination of the two former indices. Below normal EVI values for the types of vegetation were observed in the first semester of 2016 as a consequence of the 2015 drought.

The NASA/CNES Surface Water and Ocean Topography (SWOT) mission is to be launched in 2021 and will improve flood monitoring in Tonle Sap by providing water level maps through SAR interferometry techniques at better spatial and temporal resolutions with low impact of cloud presence and vegetation. The data will provide a better understanding of the strong relationship between climatic indices and Tonle Sap lake volume extreme changes, suggested by Räsänen and Kummu (2013) for the whole Mekong basin and therefore help in forecasting the risk of extreme droughts or floods.

Acknowledgements

This work was supported by the CNES, through TOSCA grants attributed to the “Variabilité hydro-sédimentaire du bassin hydrologique du MEKONG par télédétection (VolTransMesKong)” project and to the “Centre de Topographie de l'Océan et de l'Hydrosphère (CTOH)”. It is based on observations with nadir radar altimeters on board Topex/Poseidon, Jason-1, Jason-2, Jason-3, ERS-2, ENVISAT, and SARAL satellites and with MODIS instruments on board Terra and Aqua satellites. C. Normandin is supported by a PhD grant from Ministère de l'Enseignement Supérieur et de la Recherche. The Mekong River Commission (MRC) is also warmly thanked for providing on its website (www.mrcmekong.org) many resources concerning the Mekong basin. We thank Dr. S. Calmant, Dr. J.-F. Crétaux and two anonymous reviewers for their very useful comments that helped improve this manuscript.

Appendix A. Supplementary data

Supplementary data to this article can be found online at https://doi.org/10.1016/j.scitotenv.2018.04.326.

References

Adrian, R., O'Reilly, C.M., Zagarese, H., Baines, S.B., Hessen, D.O., Keller, W., Livingstone, D.M., Sommaruga, R., Straile, D., Van Donk, E., Weyhenmeyer, G.A., Winder, M., 2009. Lakes as sentinels of climate change. Limnol. Oceanogr. 54:2283–2297. https://doi.org/10.4319/lo.2009.54.6_part_2.2283.

Arias, M.E., Cochrane, T.A., Piman, T., Kummu, M., Caruso, B.S., Killeen, T.J., 2012. Quantifying changes in flooding and habitats in the Tonle Sap Lake (Cambodia) caused by water infrastructure development and climate change in the Mekong Basin. J. Environ. Manag. 112:53–66. https://doi.org/10.1016/j.jenvman.2012.07.003.

Arias, M.E., Cochrane, T.A., Norton, D., Killeen, T.J., Khon, P., 2013. The flood pulse as the underlying driver of vegetation in the largest wetland and fishery of the Mekong Basin. Ambio 42 (7):864–876. https://doi.org/10.1007/s13280-013-0424-4.

Arias, M.E., Cochrane, T.A., Kummu, M., Lauri, H., Holtgrieve, G.W., Koponen, J., Piman, T., 2014. Impacts of hydropower and climate change on drivers of ecological productivity of Southeast Asia's most important wetland. Ecol. Model. 272:252–263. https://doi.org/10.1016/j.ecolmodel.2013.10.015.

Baup, F., Frappart, F., Maubant, J., 2014. Combining high-resolution satellite images and altimetry to estimate the volume of small lakes. Hydrol. Earth Syst. Sci. 18:2007–2020. https://doi.org/10.5194/hess-18-2007-2014.

Biancamaria, S., Frappart, F., Leleu, A.-S., Marieu, V., Blumstein, D., Desjonquères, J.-D., Boy, F., Sottolichio, A., Valle-Levinson, A., 2017. Satellite radar altimetry water elevations performance over a 200 m wide river: evaluation over the Garonne River. Adv. Space Res. 59:128–146. https://doi.org/10.1016/j.asr.2016.10.008.

Broxton, P.D., Zeng, X., Sulla-Menashe, D., Troch, P.A., 2014. A global land cover climatology using MODIS data. J. Appl. Meteorol. Climatol. 53:1593–1605. https://doi.org/10.1175/JAMC-D-13-0270.1.

Campbell, I.C., Poole, C., Giesen, W., Valbo-Jorgensen, J., 2006. Species diversity and ecology of Tonle Sap Great Lake, Cambodia. Aquat. Sci. 68:355–373. https://doi.org/10.1007/s00027-006-0855-0.

Campbell, I.C., Say, S., Beardall, J., 2009. Chapter 10 - Tonle Sap Lake, the heart of the Lower Mekong. The Mekong. Academic Press, San Diego, pp. 251–272.

Certeza Surveying, 1964. Final Report to the Committee for Coordination of Investigations of the Lower Mekong Basin. Certeza, Quezon City, The Philippines.

Crétaux, J.-F., Biancamaria, S., Arsen, A., Bergé-Nguyen, M., Becker, M., 2015. Global surveys of reservoirs and lakes from satellites and regional application to the Syrdarya river basin. Environ. Res. Lett. 10:015002. https://doi.org/10.1088/1748-9326/10/1/015002.

Crétaux, J.-F., Abarca-del-Río, R., Bergé-Nguyen, M., Arsen, A., Drolon, V., Clos, G., Maisongrande, P., 2016. Lake volume monitoring from space. Surv. Geophys. 37: 269–305. https://doi.org/10.1007/s10712-016-9362-6.

Crétaux, J.-F., Nielsen, K., Frappart, F., Papa, F., Calmant, S., Benveniste, J., 2017. Hydrological applications of satellite altimetry: rivers, lakes, man-made reservoirs, inundated areas. In: Stammer, D., Cazenave, A. (Eds.), Satellite Altimetry Over Oceans and Land Surfaces, Earth Observation of Global Changes. CRC Press.

Cruz, R.V., Harasawa, H., Lal, M., Wu, S., Anokhin, Y., Punsalmaa, B., Honda, Y., Jafari, M., Li, C., Huu Ninh, N., 2007. Asia. Climate change 2007: impacts, adaptation and vulnerability. In: Parry, M.L., Canziani, O.F., Palutikof, J.P., van der Linden, P.J., Hanson, C.E. (Eds.), Contribution of Working Group II to the Fourth Assessment Report of the Intergovernmental Panel on Climate Change. Cambridge University Press, Cambridge, UK, pp. 469–506.

Delgado, J.M., Merz, B., Apel, H., 2012. A climate-flood link for the lower Mekong River. Hydrol. Earth Syst. Sci. 16:1533–1541. https://doi.org/10.5194/hess-16-1533-2012.

Farr, T.G., Rosen, P.A., Caro, E., Crippen, R., Duren, R., Hensley, S., Kobrick, M., Paller, M., Rodriguez, E., Roth, L., Seal, D., Shaffer, S., Shimada, J., Umland, J., Werner, M., Oskin, M., Burbank, D., Alsdorf, D., 2007. The shuttle radar topography mission. Rev. Geophys. 45. https://doi.org/10.1029/2005RG000183.

Fayne, J.V., Bolten, J.D., Doyle, C.S., Fuhrmann, S., Rice, M.T., Houser, P.R., Lakshmi, V., 2017. Flood mapping in the lower Mekong River Basin using daily MODIS observations. Int. J. Remote Sens. 38:1737–1757. https://doi.org/10.1080/01431161.2017.1285503.

Frappart, F., Calmant, S., Cauhopé, M., Seyler, F., Cazenave, A., 2006a. Preliminary results of ENVISAT RA-2-derived water levels validation over the Amazon basin. Remote Sens. Environ. 100:252–264. https://doi.org/10.1016/j.rse.2005.10.027.

Frappart, F., Minh, K.D., L'Hermitte, J., Cazenave, A., Ramillien, G., Le Toan, T., Mognard-Campbell, N., 2006b. Water volume change in the lower Mekong from satellite altimetry and imagery data. Geophys. J. Int. 167:570–584. https://doi.org/10.1111/j.1365-246X.2006.03184.x.

Frappart, F., Fatras, C., Mougin, E., Marieu, V., Diepkilé, A.T., Blarel, F., Borderies, P., 2015a. Radar altimetry backscattering signatures at Ka, Ku, C, and S bands over West Africa. Phys. Chem. Earth Parts ABC 83–84:96–110. https://doi.org/10.1016/j.pce.2015.05.001.

Frappart, F., Papa, F., Marieu, V., Malbeteau, Y., Jordy, F., Calmant, S., Durand, F., Bala, S., 2015b. Preliminary assessment of SARAL/AltiKa observations over the Ganges-Brahmaputra and Irrawaddy rivers. Mar. Geod. 38:568–580. https://doi.org/10.1080/01490419.2014.990591.

Frappart, F., Roussel, N., Biancale, R., Martinez Benjamin, J.J., Mercier, F., Perosanz, F., Garate Pasquin, J., Martin Davila, J., Perez Gomez, B., Gracia Gomez, C., Lopez Bravo, R., Tapia Gomez, A., Gili Ripoll, J., Hernandez Pajares, M., Salazar Lino, M., Bonnefond, P., Valles Casanova, I., 2015c. The 2013 Ibiza calibration campaign of Jason-2 and SARAL altimeters. Mar. Geod. 38:219–232. https://doi.org/10.1080/01490419.2015.1008711.

Frappart, F., Legrésy, B., Niño, F., Blarel, F., Fuller, N., Fleury, S., Birol, F., Calmant, S., 2016. An ERS-2 altimetry reprocessing compatible with ENVISAT for long-term land and ice sheets studies. Remote Sens. Environ. 184:558–581. https://doi.org/10.1016/j.rse.2016.07.037.

Hortle, K.G., 2007. Consumption and the yield of fish and other aquatic animals from the Lower Mekong Basin. MRC Technical Paper No16. Mekong River Commission, Vientiane (87 pp. ISSN: 1383-1489).

Huete, A., 1997. A comparison of vegetation indices over a global set of TM images for EOS-MODIS. Remote Sens. Environ. 59:440–451. https://doi.org/10.1016/S0034-4257(96)00112-5.

Huffman, G.J., Adler, R.F., Bolvin, D.T., Nelkin, E.J., 2010. The TRMM Multi-Satellite Precipitation Analysis (TMPA). In: Gebremichael, M., Hossain, F. (Eds.), Satellite Rainfall Applications for Surface Hydrology. Springer Netherlands, Dordrecht:pp. 3–22 https://doi.org/10.1007/978-90-481-2915-7_1.

Junk, W.J., Brown, M., Campbell, I.C., Finlayson, M., Gopal, B., Ramberg, L., Warner, B.G., 2006. The comparative biodiversity of seven globally important wetlands: a synthesis. Aquat. Sci. 68:400–414. https://doi.org/10.1007/s00027-006-0856-z.

Kamoshita, A., Ouk, M., 2015. Field level damage of deepwater rice by the 2011 Southeast Asian Flood in a flood plain of Tonle Sap Lake, Northwest Cambodia. Paddy Water Environ. 13:455–463. https://doi.org/10.1007/s10333-014-0463-x.

Kim, J.-W., Yeh, S.-W., Chang, E.-C., 2014. Combined effect of El Niño-Southern Oscillation and Pacific Decadal Oscillation on the East Asian winter monsoon. Clim. Dyn. 42: 957–971. https://doi.org/10.1007/s00382-013-1730-z.

Kummu, M., Sarkkula, J., 2008. Impact of the Mekong River flow alteration on the Tonle Sap flood pulse. AMBIO J. Hum. Environ. 37:185–192. https://doi.org/10.1579/0044-7447(2008)37[185:IOTMRF]2.0.CO;2.

Kummu, M., Sarkkula, J., Koponen, J., Nikula, J., 2006. Ecosystem management of the Tonle Sap Lake: an integrated modelling approach. Int. J. Water Resour. Dev. 22:497–519. https://doi.org/10.1080/07900620500482915.

Kummu, M., Tes, S., Yin, S., Adamson, P., Józsa, J., Koponen, J., Richey, J., Sarkkula, J., 2014. Water balance analysis for the Tonle Sap lake – floodplain system. Hydrol. Process. 28 (4):1722–1733. https://doi.org/10.1002/hyp.9718.

Lamb, P.J., 1982. Persistence of Subsaharan drought. Nature 299:46–48. https://doi.org/10.1038/299046a0.

Lamberts, D., 2006. The Tonle Sap Lake as a productive ecosystem. Int. J. Water Resour. Dev. 22:481–495. https://doi.org/10.1080/07900620500482592.

Lemoalle, J., Bader, J.-C., Leblanc, M., Sedick, A., 2012. Recent changes in Lake Chad: observations, simulations and management options (1973–2011). Glob. Planet. Chang. 80–81:247–254. https://doi.org/10.1016/j.gloplacha.2011.07.004.

Lim, P., Lek, S., Touch, S.T., Mao, S.-O., Chhouk, B., 1999. Diversity and spatial distribution of freshwater fish in Great Lake and Tonle Sap river (Cambodia, Southeast Asia). Aquat. Living Resour. 12:379–386. https://doi.org/10.1016/S0990-7440(99)00107-2.

Liu, B., Zhu, C., Su, J., Hua, L., Duan, Y., 2017. Why was the western Pacific subtropical anticyclone weaker in late summer after the 2015/2016 super El Niño?: weakened WPSA following the 2015/2016 super EL Niño. Int. J. Climatol. https://doi.org/10.1002/joc.5160.

Lu, X.X., Li, S., Kummu, M., Padawangi, R., Wang, J.J., 2014. Observed changes in the water flow at Chiang Saen in the lower Mekong: impacts of Chinese dams? Quat. Int. 336: 145–157. https://doi.org/10.1016/j.quaint.2014.02.006.

Magnuson, J.J., 2000. Historical trends in lake and river ice cover in the northern hemisphere. Science 289:1743–1746. https://doi.org/10.1126/science.289.5485.1743.

Mantua, N.J., Hare, S.R., Zhang, Y., Wallace, J.M., Francis, R.C., 1997. A Pacific interdecadal climate oscillation with impacts on salmon production. Bull. Am. Meteorol. Soc. 78:1069–1079. https://doi.org/10.1175/1520-0477(1997)078<1069:APICOW>2.0.CO;2.

MRC, 1999. Hydrographic Atlas of 1999 for the Tonle Sap River and the Tonle Sap Lake. Mekong River Commission (MRC), Phnom Penh, Cambodia.

MRC, 2003. State of the Basin Report: 2003. Mekong River Commission, Phnom Penh, Cambodia (316 pp. ISSN: 1728–3248).

MRC, 2005. Overview of the Hydrology of the Mekong Basin. 2005. Mekong River Commission, Vientiane, p. 82 (November).

Newman, M., Compo, G.P., Alexander, M.A., 2003. ENSO-forced variability of the Pacific decadal oscillation. J. Clim. 16:3853–3857. https://doi.org/10.1175/1520-0442(2003)016<3853:EVOTPD>2.0.CO;2.

Normandin, C., Frappart, F., Lubac, B., Bélanger, S., Marieu, V., Blarel, F., Robinet, A., Guiastrennec-Faugas, L., 2018. Quantification of surface water volume changes in the Mackenzie Delta using satellite multi-mission data. Hydrol. Earth Syst. Sci. 22: 1543–1561. https://doi.org/10.5194/hess-22-1543-2018.

Rainboth, W.J., 1996. Fishes of the Cambodian Mekong. FAO Species Identification Field Guide for Fishery Purposes. FAO, Rome 92-5-103743-4.

Räsänen, T.A., Kummu, M., 2013. Spatiotemporal influences of ENSO on precipitation and flood pulse in the Mekong River Basin. J. Hydrol. 476:154–168. https://doi.org/10.1016/j.jhydrol.2012.10.028.

Rayner, N.A., 2003. Global analyses of sea surface temperature, sea ice, and night marine air temperature since the late nineteenth century. J. Geophys. Res. 108. https://doi.org/10.1029/2002JD002670.

Rosenzweig, C., Casassa, G., Karoly, D.J., Imeson, A., Liu, C., Menzel, A., Rawlins, S., Root, T.L., Seguin, B., Tryjanowski, P., 2007. Assessment of observed changes and responses in natural and managed systems. In: Parry, M.L., Canziani, O.F., Palutikof, J.P., van der Linden, P.J., Hanson, C.E. (Eds.), Climate Change 2007: Impacts, Adaptation and Vulnerability. Contribution of Working Group II to the Fourth Assessment Report of the Intergovernmental Panel on Climate Change. Cambridge University Press, Cambridge, UK, pp. 79–131.

Sakamoto, T., Van Nguyen, N., Kotera, A., Ohno, H., Ishitsuka, N., Yokozawa, M., 2007. Detecting temporal changes in the extent of annual flooding within the Cambodia and the Vietnamese Mekong Delta from MODIS time-series imagery. Remote Sens. Environ. 109:295–313. https://doi.org/10.1016/j.rse.2007.01.011.

Santos da Silva, J., Calmant, S., Seyler, F., Rotunno Filho, O.C., Cochonneau, G., Mansur, W.J., 2010. Water levels in the Amazon basin derived from the ERS 2 and ENVISAT radar altimetry missions. Remote Sens. Environ. 114:2160–2181. https://doi.org/10.1016/j.rse.2010.04.020.

Schindler, D.W., 2009. Lakes as sentinels and integrators for the effects of climate change on watersheds, airsheds, and landscapes. Limnol. Oceanogr. 54:2349–2358. https://doi.org/10.4319/lo.2009.54.6_part_2.2349.

Siev, S., Paringit, E., Yoshimura, C., Hul, S., 2016. Seasonal changes in the inundation area and water volume of the Tonle Sap River and its floodplain. Hydrology 3:33. https://doi.org/10.3390/hydrology3040033.

Stone, R., 2010. Severe drought puts spotlight on Chinese dams. Science 327:1311. https://doi.org/10.1126/science.327.5971.1311.

Sverdrup-Jensen, S., 2002. Fisheries in the Lower Mekong Basin: status and perspectives. MRC Technical Paper No6. Phnom Penh, Mekong River Commission (130 pp. ISSN: 1683-1489).

Tangdamrongsub, N., Ditmar, P.G., Steele-Dunne, S.C., Gunter, B.C., Sutanudjaja, E.H., 2016. Assessing total water storage and identifying flood events over Tonlé Sap basin in Cambodia using GRACE and MODIS satellite observations combined with hydrological models. Remote Sens. Environ. 181:162–173. https://doi.org/10.1016/j.rse.2016.03.030.

UNESCO, 2006. Biosphere Reserves - World Network. UNESCO - MAB Secretariat, Paris, France Available at:. http://www.unesco.org/mab/.

Västilä, K., Kummu, M., Sangmanee, C., Chinvanno, S., 2010. Modelling climate change impacts on the flood pulse in the Lower Mekong floodplains. J. Water Clim. Change 01: 67. https://doi.org/10.2166/wcc.2010.008.

Vu, P.-L., Frappart, F., Darrozes, J., Marieu, V., Blarel, F., Ramillien, G., Bonnefond, P., Birol, F., 2018. Multi-satellite altimeter validation along the French Atlantic Coast in the

southern Bay of Biscay from ERS-2 to SARAL. Remote Sens. 10 (1):93. https://doi.org/10.3390/rs10010093.

Wang, B., Fan, Z., 1999. Choice of south Asian summer monsoon indices. Bull. Am. Meteorol. Soc. 80:629–638. https://doi.org/10.1175/1520-0477(1999)080<0629:COSASM>2.0.CO;2.

Wang, B., Wu, R., Lau, K.-M., 2001. Interannual variability of the Asian summer monsoon: contrasts between the Indian and the western North Pacific–East Asian monsoons. J. Clim. 14:4073–4090. https://doi.org/10.1175/1520-0442(2001)014<4073:IVOTAS>2.0.CO;2.

Williamson, C.E., Saros, J.E., Schindler, D.W., 2009a. Climate change: sentinels of change. Science 323:887–888. https://doi.org/10.1126/science.1169443.

Williamson, C.E., Saros, J.E., Vincent, W.F., Smol, J.P., 2009b. Lakes and reservoirs as sentinels, integrators, and regulators of climate change. Limnol. Oceanogr. 54:2273–2282. https://doi.org/10.4319/lo.2009.54.6_part_2.2273.

WUP-FIN, 2003. Modelling Tonle Sap for Environmental Impact Assessment and Management Support, MRCS/WUP-FIN Project. Final Report. Mekong River Commission, Phnom Penh.